Article

Ligand K-edge X-ray Absorption Spectroscopy and DFT Calculations on [FeS] Clusters: Delocalization, Redox, and Effect of the Protein Environment

Abhishek Dey, Thorsten Glaser, Jose J.-G. Moura, Richard H. Holm, Britt Hedman, Keith O. Hodgson, and Edward I. Solomon

J. Am. Chem. Soc., **2004**, 126 (51), 16868-16878• DOI: 10.1021/ja0466208 • Publication Date (Web): 07 December 2004

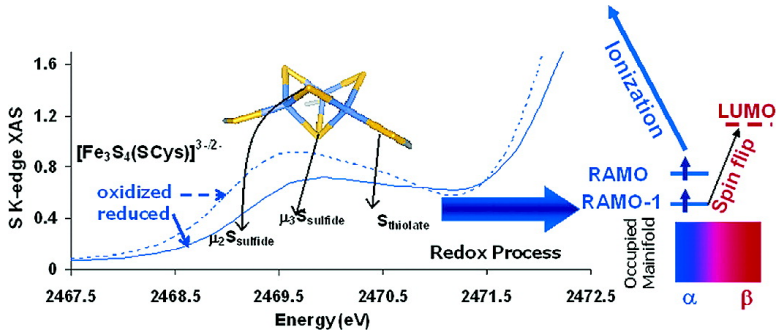

More About This Article

Additional resources and features associated with this article are available within the HTML version:

- Supporting Information
- Links to the 2 articles that cite this article, as of the time of this article download
- Access to high resolution figures
- Links to articles and content related to this article
- Copyright permission to reproduce figures and/or text from this article

View the Full Text HTML

J|A|C|S
ARTICLES
Published on Web 12/07/2004

Ligand K-edge X-ray Absorption Spectroscopy and DFT Calculations on $[Fe_3S_4]^{0,+}$ Clusters: Delocalization, Redox, and Effect of the Protein Environment

Abhishek Dey,[†] Thorsten Glaser,[||] Jose J.-G. Moura,[‡] Richard H. Holm,[§] Britt Hedman,*[,⊥] Keith O. Hodgson,*[,†,⊥] and Edward I. Solomon*[,†]

Contribution from the Department of Chemistry and Stanford Synchrotron Radiation Laboratory, Stanford University, Stanford, California 94305; Departmento de Quimica, Universidade Nova de Lisboa, Portugal; Department of Chemistry and Chemical Biology, Harvard University, Cambridge, Massachusetts 02138

Received June 8, 2004; E-mail: hedman@ssrl.slac.stanford.edu; Edward.solomon@stanford.edu

Abstract: Ligand K-edge XAS of an $[Fe_3S_4]^0$ model complex is reported. The pre-edge can be resolved into contributions from the $\mu_2S_{sulfide}$, $\mu_3S_{sulfide}$, and $S_{thiolate}$ ligands. The average ligand−metal bond covalencies obtained from these pre-edges are further distributed between Fe^{3+} and $Fe^{2.5+}$ components using DFT calculations. The bridging ligand covalency in the $[Fe_2S_2]^+$ subsite of the $[Fe_3S_4]^0$ cluster is found to be significantly lower than its value in a reduced $[Fe_2S_2]$ cluster (38% vs 61%, respectively). This lowered bridging ligand covalency reduces the superexchange coupling parameter J relative to its value in a reduced $[Fe_2S_2]^+$ site (-146 cm^{-1} vs -360 cm^{-1}, respectively). This decrease in J, along with estimates of the double exchange parameter B and vibronic coupling parameter λ^2/k_-, leads to an $S = 2$ delocalized ground state in the $[Fe_3S_4]^0$ cluster. The S K-edge XAS of the protein ferredoxin II (Fd II) from the *D. gigas* active site shows a decrease in covalency compared to the model complex, in the same oxidation state, which correlates with the number of H-bonding interactions to specific sulfur ligands present in the active site. The changes in ligand−metal bond covalencies upon redox compared with DFT calculations indicate that the redox reaction involves a two-electron change (one-electron ionization plus a spin change of a second electron) with significant electronic relaxation. The presence of the redox inactive Fe^{3+} center is found to decrease the barrier of the redox process in the $[Fe_3S_4]$ cluster due to its strong antiferromagnetic coupling with the redox active Fe_2S_2 subsite.

Introduction

Iron−sulfur clusters are found in the active sites of many metalloenzymes in both higher and lower organisms. Their main biological function is one-electron transfer. The most widely distributed active-site cluster types are mononuclear, in rubredoxins, binuclear, in plant ferredoxins and tetranuclear, in bacterial ferredoxin and HiPiP proteins.[1] The different structural motifs and the wide range in redox potential, from −650 mV to +500 mV,[2] make these proteins very versatile electron transport agents in biological systems. The electronic structures of these clusters have been studied using different spectroscopic techniques and DFT calculations.[3−5]

In addition to the common Fe−S sites mentioned above, trinuclear $[Fe_3S_4]$ clusters are found in proteins such as ferredoxin II from *D. gigas* and ferredoxin protein from *A. vinelandii*.[6,7] In some cases their biological functions are not clear, but in the above proteins the $[Fe_3S_4]$ sites are believed to function in electron transport. These active sites have adjacent irons bridged by one $\mu_2S_{sulfide}$; all three iron atoms also share a $\mu_3S_{sulfide}$ (Figure 1) and each iron atom has a terminal $S_{thiolate}$ bond. The oxidized cluster has three high spin ferric centers giving a spin frustrated $S = {}^1/_2$ state.[8] In the reduced state, a high spin ferric center $S = {}^5/_2$ is antiferromagnetically coupled to a valence delocalized $[Fe_2S_2]^+$ $S = {}^9/_2$ subsite to give an $S =$

[†] Stanford University.
[||] Present address: Institut für Anorganische und Analytische Chemie, Westfaelische Wilhelms-Universität Muenster, Germany.
[‡] Universidade Nova de Lisboa.
[§] Harvard University.
[⊥] Stanford Synchrotron Radiation Laboratory, SLAC, Menlo Park, CA, 94025.

(1) (a) *Iron−Sulfur Proteins*; Lovenberg, W., Ed.; Academic Press: New York, 1973−1977; Vols. I−III. (b) *Iron−Sulfur Proteins*; Spiro, T. G., Ed.; Metal Ions In Biology; Wiley-Interscience: New York, 1982; Vol. IV. (c) *Iron−Sulfur Proteins*; Cammack, R., Ed.; Advances in Inorganic Chemistry; Academic Press: San Diego, 1992; Vol. 38. (d) *Iron−Sulfur Proteins*; Sykes, A. G.; Cammack, R.; Eds.; Advances in Inorganic Chemistry; Academic Press: San Diego, 1999; Vol. 47
(2) Stephens, P. J.; Jollie, D. R.; Warshel, A. *Chem. Rev.* **1996**, *96*, 2491−2514.
(3) Holm, R. H.; Averill, B. A.; Herskovitz, T.; Frankel, R. B.; Gray, H. B.; Siiman, O.; Grunthaner, F. J. *J. Am. Chem. Soc.* **1974**, *96*, 2644−2646.
(4) Czernuszewicz, R. S.; Macor, K. A.; Johnson, M. K.; Gewirth, A.; Spiro, T. G. *J. Am. Chem. Soc.* **1987**, *109*, 7178−7187.
(5) Noodleman, L.; Norman, J. G.; Osborne, J. H.; Aizman, A.; Case, D. A. *J. Am. Chem. Soc.* **1985**, *107*, 3418−3426.
(6) Kissinger, C. R.; Sieker, L. C.; Adman, E. T.; Jensen, L. H. *J. Mol. Biol.* **1991**, *219*, 693−715.
(7) Schipke, C. G.; Goodin, D. B.; McRee, D. E.; Stout, C. D. *Biochemistry* **1999**, *38*, 8228−8293.
(8) Hu, Z.; Jollie, D.; Burgess, B. K.; Stephens, P. J.; Munck, E. *Biochemistry* **1994**, *33*, 14475−14485.

10.1021/ja0466208 CCC: $27.50

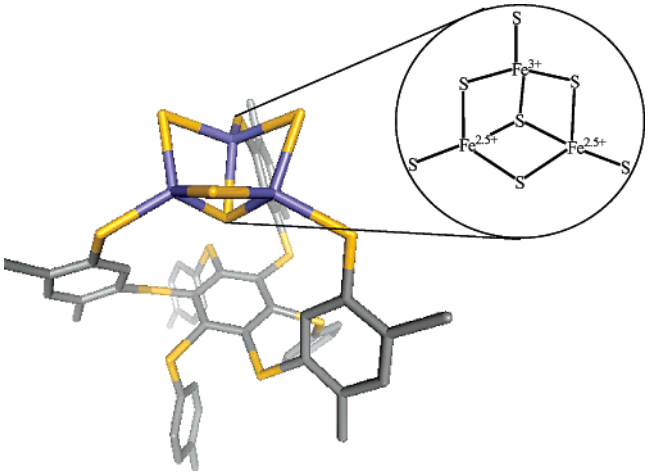

Figure 1. $[Fe_3S_4]^0$ cluster present in the complex $[NEt_4]_3[Fe_3S_4LS_3]$.

2 ground state.[9] This delocalization is also present in the $[Fe_4S_4]^{1+,2+,3+}$ clusters. However, in contrast, the reduced $[Fe_2S_2]^+$ centers in plant ferredoxins are localized.[10,11] This dramatic difference in ground state (delocalization/localization) can have contributions from several physical interactions.

Delocalization of the excess electron in the mixed-valence state is accompanied by a net ferromagnetic coupling between the iron centers leading to an $S_T = {}^9/_2$ dimer ground state.[10] This phenomenon of spin alignment in mixed-valence systems with delocalized ground states is called double exchange in analogy to Kramer's superexchange mechanism.[12] The physical origin of double exchange as elucidated by Girerd, Münck, and co-workers and by Noodleman and Baerends is that electron delocalization leads to a loss of spin polarization energy for the antiferromagnetic but not for the ferromagnetic configuration.[13,14]

There are three interactions to consider between the magnetic centers in a mixed-valence pair, namely the above-mentioned double exchange (parametrized by B), superexchange (parametrized by J (using $H = -2J\mathbf{S}_1\mathbf{S}_2$)), and vibronic coupling (Λ^2/k_- where $\Lambda^2/k_- = 4\pi^2c^2Mv_-n(\Delta r)^2$, where M is the reduced mass of the x_- mode, v_- is the frequency of the antisymmetric combination of breathing modes on both Fe, n is number of ligands, and Δr = metal−ligand bond length distortion with oxidation). The energies of the different spin states (S_T) are given by

$$E_{\pm}(S_T) = -JS_T(S_T+1) + \frac{1}{2}\left(\frac{\Lambda^2}{k_-}\right)x_-{}^2 \pm \sqrt{\frac{1}{2}\left(\frac{\Lambda^2}{k_-}\right)^2 x_-{}^2 + B^2\left(S_T+\frac{1}{2}\right)^2} \quad (1)$$

where x_- is the dimensionless antisymmetric breathing mode of the $[Fe_2S_2]$ unit which may be an isolated cluster in case of plant ferredoxin or may be a part of a higher nuclearity cluster as in the case of bacterial ferredoxins and HiPIPs.

Superexchange leads to antiferromagnetic coupling, whereas double exchange leads to delocalization of the excess electron and thus ferromagnetic coupling. Vibronic coupling is the driving force for localization of the extra electron. The interplay among these three interactions leads to interesting potential energy surfaces for the spin states in the antisymmetric breathing mode x_-. From eq 1, double exchange, as the driving force for electron delocalization, is more effective in the higher spin states (proportional to $(S_T + {}^1/_2)$). Thus, strong superexchange, which leads to antiferromagnetic coupling and stabilization of the lower spin states, makes the double exchange less effective and thus decreases the tendency for electron delocalization.

It has been considered that the delocalization of the extra electron in the mixed-valence dimer subsites of $[Fe_3S_4]^0$ and $[Fe_4S_4]^{1+,2+,3+}$ results from spin frustration.[15,50] The spins in these clusters cannot all be aligned antiferromagnetically due

(9) Weigel, J. A.; Holm, R. H.; Surerus, K. K.; Munck, E. *J. Am. Chem. Soc.* **1989**, *111*, 9246−9247.
(10) Beinert, H.; Holm, R. H.; Munck, E. *Science* **1997**, *277*, 653−659.
(11) Note that some Cys → Ser mutants of *Cp* ferredoxins show a delocalized $S = {}^9/_2$ ground state. Crouse, B. R.; Meyer, J.; Johnson, M. K. *J. Am. Chem. Soc.* **1995**, *117*, 9612−9613.
(12) Kramer, A. *Physica* **1934**, *1*, 191−192.
(13) Blondin, G.; Girerd, J.-J. *Chem. Rev.* **1990**, *90*, 1359−1376.
(14) Noodleman, L.; Baereands, E. J. *J. Am. Chem. Soc.* **1984**, *106*, 2316−2327.
(15) Toulouse, G. *Commun. Phys.* (London) **1977**, *2*, 115.
(16) Girerd, J.-J. *J. Chem. Phys.* **1983**, *79*, 1766−1775.
(17) Blondin, G.; Borshch, S. A.; Girerd, J.-J. *Comments Inorg. Chem.* **1992**, *12*, 315−340.
(18) Borshch, S. A.; Bominaar, E. L.; Blondin, G.; Girerd, J.-J *J. Am. Chem. Soc.* **1993**, *115*, 5155−5168.
(19) Ding, X.-Q.; Bominaar, E. L.; Bill, E.; Winkler, H.; Trautwein, A. X.; Druëke, S.; Chaudhuri, P.; Wieghardt, K. *J. Chem. Phys.* **1990**, *92*, 178−186.
(20) Gamelin, D. R.; Bominaar, E. L.; Mathoniere, C.; Kirk, M. L.; Wieghardt, K.; Girerd, J.-J.; Solomon, E. I. *Inorg. Chem.* **1996**, *35*, 4323−4335.
(21) Glaser, T.; Rose, K.; Shadle, S. E.; Hedman, B.; Hodgson, K. O.; Solomon, E. I. *J. Am. Chem. Soc.* **2001**, *123*, 442−454.
(22) Glaser, T. T.; Hedman, B.; Hodgson, K. O.; Solomon, E. I. *Acc. Chem. Res.* **2000**, *33*, 859−868.
(23) Neese, F. F.; Hedman, B.; Hodgson, K. O.; Solomon, E. I. *Inorg. Chem.* **1999**, *38*, 4854−4860.
(24) Rose, K.; Shadle, S. E.; Eidsness, M. K.; Kurtz, D. M., Jr.; Scott, R. A.; Hedman, B.; Hodgson, K. O.; Solomon, E. I. *J. Am. Chem. Soc.* **1998**, *120*, 10743−10747.
(25) (a) Rose, K.; Shadle, S.; Glaser, T.; de Vries, S.; Cherepanov, A.; Canters, G. W.; Hedman, B.; Hodgson, K. O.; Solomon, E. I. *J. Am. Chem. Soc.* **1999**, *121*, 2353−2363. (b) Anxolabéhère-Mallart, E.; Glaser, T.; Frank, P.; Aliverti, A.; Zanetti, G.; Hedman, B.; Hodgson, K. O.; Solomon, E. I. *J. Am. Chem. Soc.* **2001**, *123*, 5444−5452.
(26) Dey, A.; Glaser, T.; Couture, M. M.-J.; Eltis, L. D.; Holm, R. H.; Hedman, B.; Hodgson, K. O.; Solomon, E. I. *J. Am. Chem. Soc.* **2004**, *126*, 8320−8328.
(27) Zhou, J.; Hu, Z.; Munck, E.; Holm, R. H. *J. Am. Chem. Soc.* **1996**, *118*, 1966−1980.
(28) Macedo, A. L.; Moura, I.; Surerus, K. K.; Papaefthymiou, V.; Liu, M. Y.; LeGall, J.; Munck, E.; Moura, J. J. *J. Biol. Chem.* **1994**, *269*, 8052−8058.
(29) Hedman, B.; Frank, P.; Gheller, S. F.; Roe, A. L.; Newton, W. E.; Hodgson, K. O. *J. Am. Chem. Soc.* **1988**, *110*, 3798−3805.
(30) Agarwal, B. K. In *X-ray Spectroscopy*; Springer-Verlag: Berlin, 1979.
(31) Tyson, T. A.; Roe, A. L.; Frank, P.; Hodgson, K. O.; Hedman, B. *Phys. Rev. B* **1989**, *39A*, 6305−6315.
(32) Baerends, E. J.; Ellis, D. E.; Ros, P. *Chem. Phys.* **1973**, *2*, 41−51.
(33) Vosko, S. H.; Wilk, L.; Nusair, M. *Can. J. Phys.* **1980**, *58*, 1200−1211.
(34) Becke, A. D. *J. Chem. Phys.* **1986**, *84*, 4524−4529.
(35) Perdew, J. P. *Phys. Rev. B* **1986**, *33*, 8822−8824.
(36) Noodleman, L. *J. Chem. Phys.* **1981**, *74*, 5737−5743.
(37) Shadle, S. E.; Hedman, B.; Hodgson K. O.; Solomon, E. I. *Inorg. Chem.* **1994**, *33*, 4235−4244.
(38) Note that in single-point calculations as the Fe−$S_{thiolate}$ bond lengths decrease from 2.41 Å (the optimized value) to 2.33 Å (the value in crystal structure), the energy of the system increases by only 0.1 eV.
(39) Note that the $\mu_2S_{sulfide}$ covalency reflects the average of the two different Fe−$\mu_2S_{sulfide}$ bonds present in the complex (Figure 7), the one bridging between two $Fe^{2.5+}$ centers, S_s, and two bridging an $Fe^{2.5+}$ to an Fe^{3+}, S_o.
(40) Noodleman, L.; Case, D. A. *Adv. Inorg. Chem.* **1992**, *38*, 423−470.
(41) Sanghwa, H.; Czernuszewicz, R. S.; Spiro, T. G. *J. Am. Chem. Soc.* **1989**, *111*, 3496−3504.
(42) (a) The vibronic coupling constant was estimated to be 2800 cm^{-1} by using Mossbauer spectroscopy and the temp dependence of the magnetic susceptibility in *B*. (b) Eremin, M. V.; Nikitin, S. I.; Prosvirnin, S. Yu. *App. Magn. Res.* **2002**, *23*, 97−104.
(43) (a) Note that crystal structures of *A. vinelandii* show that change in geometry on oxidation is insignificant (ref 43b). Thus geometric relaxation has been neglected in the analysis. (b) Stout C. D. *J. Biol. Chem.* **1993**, *268*, 25920−25927.
(44) Chen, B.; Menon, N. K.; Dervertarnian, L.; Moura, J. J. G.; Przybyla, A. E. *FEBS Lett.* **1994**, *351*, 401−404.

to the presence of three or four bridged spin centers. This spin frustration contributes to the parallel alignment of the spins. The parallel spin alignment assists the double exchange leading to the delocalized dimer subsite. It has been proposed that double exchange and vibronic coupling interactions, without superexchange coupling *J*, can lead to a delocalized ground state in these $[Fe_2S_2]^+$ subsites.[16−18]

The mixed-valence model compound $[LFe(\mu\text{-}OH)_3FeL]^{2+}$ (L = 1,4,7-trimethyl-1,4,7-triazacyclononane) synthesized by Wieghardt, Chaudhuri, and co-workers consists formally of one Fe^{3+} and one Fe^{2+} ion but was shown to be a class III fully delocalized $(Fe^{2.5+})_2$ mixed-valence dimer with a ferromagnetic $S_T = {}^9/_2$ ground state.[19,20] Thus, delocalization of the excess electron with parallel spin alignment is possible without spin frustration in a dimer. A study comparing the delocalized mixed-valence model $[LFe(\mu\text{-}OH)_3FeL]^{2+}$ with the localized mixed-valence dimer $[Fe_2S_2]^+$ showed that the main difference between these two is the reduced superexchange coupling in the $[LFe(\mu\text{-}OH)_3FeL]^{2+}$ model as compared to the Fe−S dimer, due to the reduced covalency of the hydroxide bridging ligands with the metal centers.

An approximate relation between the superexchange coupling constant, *J*, and the experimentally observed bridging ligand covalency (from K-edge XAS) has been obtained using a valence bond configuration interaction (VBCI) model for superexchange, where LMCT states CI mix with the VB ground state.[21]

$$J \propto (\text{covalency})^2 \tag{2}$$

It has been found, from S K-edge studies comparing the $[Fe_2S_2]^+$ and the $[Fe_4S_4]^{2+}$ clusters, that the change in bridging ligand from μ_2 to μ_3 sulfide significantly reduces the bridging ligand covalency on the $[Fe_2S_2]^+$ subsite of the $[Fe_4S_4]^{2+}$ cluster. Through eq 2, this decrease in *J* is enough to change the ground state of the cluster from $S = {}^1/_2$ in $[Fe_2S_2]^+$ to $S = {}^9/_2$ in the $[Fe_2S_2]^+$ subsite in $[Fe_4S_4]^{2+}$ cluster.

Ligand K-edge X-ray absorption spectroscopy (XAS) provides a direct estimate of ligand−metal bond covalencies.[22] The primary transition at the ligand K-edge is the ligand 1s→4p transition. However, due to the covalent mixing of the ligand 3p orbitals into the partially occupied metal 3d antibonding orbitals of Fe, transitions to these orbitals from the filled ligand 1s orbital obtain absorption intensity as the intrinsic 1s → 3p transition of the ligand is electric-dipole allowed. The intensity of this transition depends on the ligand character in the 3d antibonding orbital (α^2), from which the covalency of the metal−ligand bond can be quantified according to

$$I(L_{1s} \rightarrow M_{3d}) = \alpha^2 I\langle L_{1s}|\mathbf{r}|\, L_{3p}\rangle \tag{3}$$

In eq 3, $I(1s \rightarrow L_{3p})$ is the transition moment integral or the intensity of a purely ligand 1s → 3p transition, which depends on the Z_{eff} of the ligand.[23] Thus the pre-edge intensity provides a direct estimate of ligand−metal bond covalency. This method has been used in the past to investigate the electronic structures of mononuclear, binuclear, and tetranuclear iron−sulfur active sites in protein and relevant model complexes.[21,24−26]

In the present study, the S K-edge XAS of an $[Fe_3S_4]^0$ model and the resting ($[Fe_3S_4]^0$) and oxidized ($[Fe_3S_4]^+$) active site of the protein ferredoxin II from *D. gigas* are reported. The three components $\mu_2S_{sulfide}$, $\mu_3S_{sulfide}$, and $S_{thiolate}$ are resolved in the XAS pre-edge. The bonding of this cluster is analyzed and compared to those of $[Fe_2S_2]^{2+}$ and $[Fe_4S_4]^{2+}$ clusters. The effect of covalency on the exchange interaction in the $[Fe_2S_2]^+$ subsite of the $[Fe_3S_4]^0$ cluster is evaluated using eqs 3 and 2 and combined with estimates of the delocalization and vibronic coupling in eq 1 to evaluate their contribution to electron delocalization in the $[Fe_2S_2]^+$ subsite. The bonding of the model complex is compared to that of the resting protein in the same redox state to evaluate the effect of the protein environment on the bonding of the cluster. Finally, the changes in bonding upon oxidation, observed experimentally, are analyzed using geometry-optimized DFT calculations, and a possible role of the redox-inactive Fe^{3+} center in this cluster is discussed.

Experimental Section

Sample Preparation. The model complexes $[Et_4N]_3[Fe_3S_4(LS_3)]$ and $[Et_4N]_3$ $[Fe_3Se_4(LS_3)]$ (where LS_3 is 1,3,5-tris((3-mercaptophenyl)thio)-2,4,6-tris(*p*-tolylthio)benzene) were prepared according to published methods.[27] For XAS experiments, sample preparations were performed in a dry, nitrogen-filled anaerobic atmosphere glovebox. The samples were ground into a fine powder and dispersed as thinly as possible on sulfur-free Mylar tape. This procedure has been verified to minimize self-absorption effects. The sample was then mounted across the window of an aluminum plate. A 6.35 μm polypropylene film window protected the solid samples from exposure to air during transfer from the glovebox to the experimental sample chamber.

The protein was extracted and prepared as described in refs 28 and 44.The reduced protein solutions (in 100 mM phosphate buffer, pH 7.3−7.6) were pre-equilibrated in a water-saturated He atmosphere for ~1 h to minimize bubble formation in the sample cell. The protein sample was oxidized before the experiments by using a 3−4-fold excess of potassium ferricyanide. The solution was then loaded via a syringe into a Pt-plated Al block sample holder sealed in front using a 6.3 μm polypropylene window.

Data Collection and Reduction. XAS data were measured at the Stanford Synchrotron Radiation Laboratory using the 54-pole wiggler beam line 6-2. Details of the experimental configuration for low energy studies and data reduction methods have been described in an earlier publication.[29]

Fitting Procedure. Pre-edge features were fit using pseudo-Voigt line shapes (sums of Lorentzian and Gaussian functions). This line shape is appropriate as the experimental features are expected to be a convolution of a Lorentzian transition envelope and a Gaussian line shape imposed by the beam-line spectrometer optics.[30,31] A fixed 1:1 ratio of Lorentzian to Gaussian contribution successfully reproduced

(45) Incomplete loading accounts for 7−10% of the observed change. This point is further illustrated by Figure S2 in the Supporting Information. The data clearly show the decrease in $\mu_2S_{sulfide}$ contribution to the pre-edge of the reduced protein relative to the model complex even when the contribution of the $\mu_3S_{sulfide}$ of the protein is scaled to the contribution of that in the model complex to account for any incomplete loading.

(46) Note that in similar active sites of some proteins which contain both Fe_3S_4 and Fe_4S_4 clusters (e.g., *A. vinelandii*), it has been found that the reduced $[Fe_3S_4]^0$ site is protonated based on MCD and electrochemical measurements. Protonation of a $\mu_2S_{sulfide}$ ligand would produce a similar decrease of ligand metal bond covalency as observed here. However it has been determined that the $[Fe_3S_4]^0$ protein from *D. gigas* does not show the protonation. See ref 47.

(47) Shen, B.; Martin, L. L.; Butt, J. N.; Armstrong, F. A.; Stout, C. D.; Jensen, G. M.; Stephens, P. J.; La Mar, G. N.; Gorst, C. M.; Burgess, B. K. *J. Biol. Chem.* **1993**, *268*, 25928−39.

(48) Factors other than H-bonding in particular dipoles around the cluster can also significantly affect redox potentials. See ref 49. However model studies (to be published) indicate that H-bonds do strongly perturb Fe−S bond covalency.

(49) Olsson, M. H. M.; Gongyi, H.; Warshel, A. *J. Am. Chem. Soc.* **2003**, *125*, 5025−5039.

(50) Pimenta, M. A.; Licinio, P. *Phy. Rev. B: Condens. Matter* **1994**, *50*, 722−726.

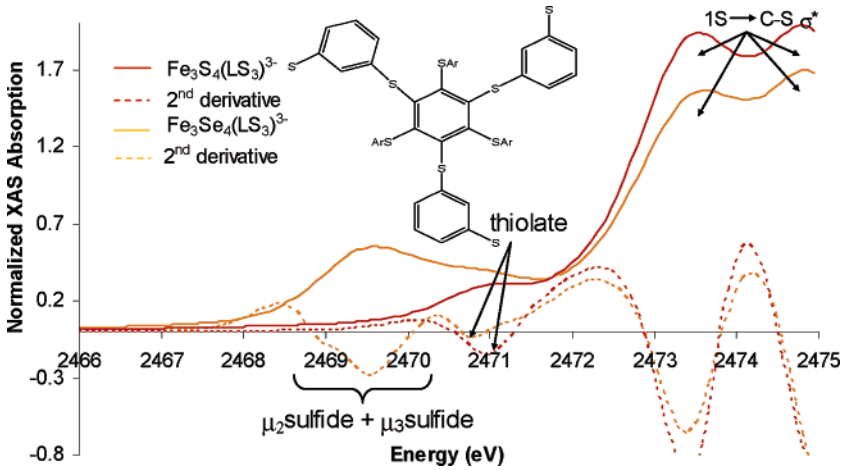

Figure 2. Normalized S K-edge XAS of $[Fe_3S_4(LS_3)]^{3-}$ (orange solid line) and its second derivative (orange dashed line) and that of $[Fe_3Se_4(LS_3)]^{3-}$ (red solid line) and its second derivative (red dashed line). Inset: the ligand LS3[ref].

the pre-edge features. The rising edge functions were also fit with pseudo-Voigt line shapes. Good fits reproduce the data using a minimum number of peaks. There are three resolvable contributions in the pre-edge region of $[Fe_3S_4(SR)_3]$ sites: $\mu_2S_{sulfide}$, $\mu_3S_{sulfide}$, and $S_{thiolate}$ (vide infra). Fits were performed using single peaks to simulate the pre-edge contributions of each component with a half-width of 0.6−0.7 eV. Fits were performed using both the same full width at half-maximum (fwhm) for all contributions or by letting their fwhm vary independently. The later procedure did not significantly change the result. The energies of the pre-edge features of the reduced model complex and of the protein were allowed to shift by 0.1−0.2 eV from the known values obtained from the previous studies (2469.5 eV for Fe^{3+}−$\mu_2S_{sulfide}$, 2470.1 for $Fe^{2.5+}$−$\mu_3S_{sulfide}$, and 2470.9 for $Fe^{2.5+}$−$S_{thiolate}$).[25,21] The intensity of a pre-edge feature (peak area) is the sum of the intensity of all the pseudo-Voigt peaks which successfully fit the feature for a given simulation. The reported intensity values for both the model complexes and the proteins represent an average of all of the good pre-edge fits, which differ from each other by less than 5%. The ligand−metal bond covalencies (per ligand) are obtained by dividing the total hole covalency of a ligand (obtained by using eq 2 in ref 15) by the number of ligand−metal bonds present in the complex (as discussed in ref 26 (a)).

DFT Calculations. All calculations were performed on IBM 3BT-RS/6000 workstations on an SGI Origin 2000 using the Amsterdam Density Functional (ADF) program versions 2002.03 and ADF 2000 developed by Baerends et al..[32] A triple-ζ Slater-type orbital basis set (ADF basis set TZP) with a single polarization function at the local density approximation of Vosko, Wilk, and Nusair[33] with nonlocal gradient corrections of Becke[34] and Perdew[35] were employed. Full optimizations were performed for all model complexes starting from crystal structures wherever available. The electronic structures of the clusters were calculated in the broken symmetry state.[36] The crystal structure for the $[Fe_2(OH)_3L_2]^{2+}$ complex was used for calculation of the delocalization parameter, *B* (vide infra), of this model complex.[19] Complete coordinates of all models presented in the text are included in the Supporting Information.

Results

A. S K-Edge XAS of Model Complexes. The S K-edge XAS spectra of $[Fe_3S_4(LS_3)]^{3-}$ (where LS_3 is 1,3,5-tris((3-mercaptophenyl)thio)-2,4,6-tris(*p*-tolylthio)benzene) and its selenide substituted analogue $[Fe_3Se_4(LS_3)]^{3-}$ are given in Figure 2 (orange and red lines, respectively). The spectrum of $[Fe_3S_4(LS_3)]^{3-}$ has two broad pre-edge features between ∼2468−2471 eV, which represent envelopes of transitions to the unoccupied metal antibonding orbitals from the 1s orbitals of the three chemically

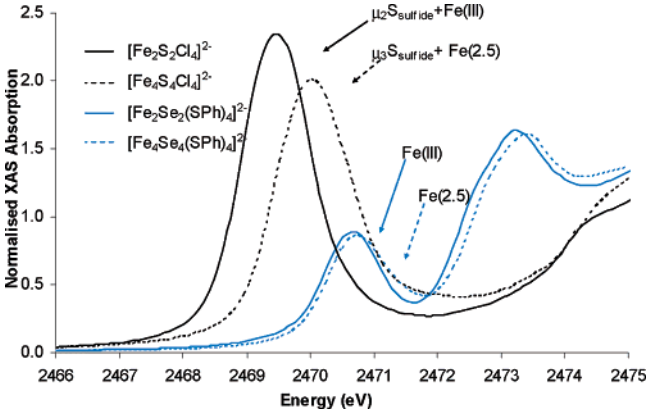

Figure 3. S K-edge XAS spectra of $[Fe_2S_2Cl_4]^{2-}$ (black solid line), $[Fe_4S_4Cl_4]^{2-}$ (black dashed line), $[Fe_2Se_2(SPh)_4]^{2-}$ (blue solid line), and $[Fe_4Se_4(SPh)_4]^{2-}$ (blue dashed line).

different types of sulfur ligands: $\mu_3S_{sulfide}$, $\mu_2S_{sulfide}$, and $S_{thiolate}$. The S K-edge of the $[Fe_3Se_4(LS_3)]^{3-}$ complex has one pre-edge feature at ∼2471 eV, assigned to the envelope of transitions from only the 1s orbitals of the ligated $S_{thiolate}$ to the unoccupied metal antibonding orbital manifold. In both complexes, there are at least two distinct rising-edge features around 2473.5 and 2474.8 eV, corresponding to sulfur 1s → C−S σ* transitions of the two different types of C−S bonds (thiolate and thioether of the ligand, Figure 1). Due to the presence of the noncovalently bound thioether sulfurs in the ligand, the normalized XAS spectra have to be renormalized (by a factor of 13/7 for the sulfide complex and 3 for the selenide complex) to account for the fact that these additional thioether sulfurs contribute to the edge jump but not to the pre-edge transitions.

The second derivative of the S K-edge XAS of these model complexes (Figure 2) allows assignment of the specific types of S contributions to the pre-edge. The second derivative of the $[Fe_3Se_4(LS_3)]^{3-}$ S K-edge XAS (Figure 2, dotted red line) data shows the presence of one feature at 2470.9 eV. Since the complex has only thiolate bound to the iron atoms, this feature corresponds to the thiolate 1s → Fe 3d (antibonding) transitions. The S K-edge XAS spectrum of $[Fe_3S_4(LS_3)]^{3-}$ shows the presence of multiple components in its pre-edge region of its second derivative (Figure 2, dotted orange line). The highest energy pre-edge feature corresponding to the minimum in the 2nd derivative at 2471.0 eV can be assigned to the thiolate 1s

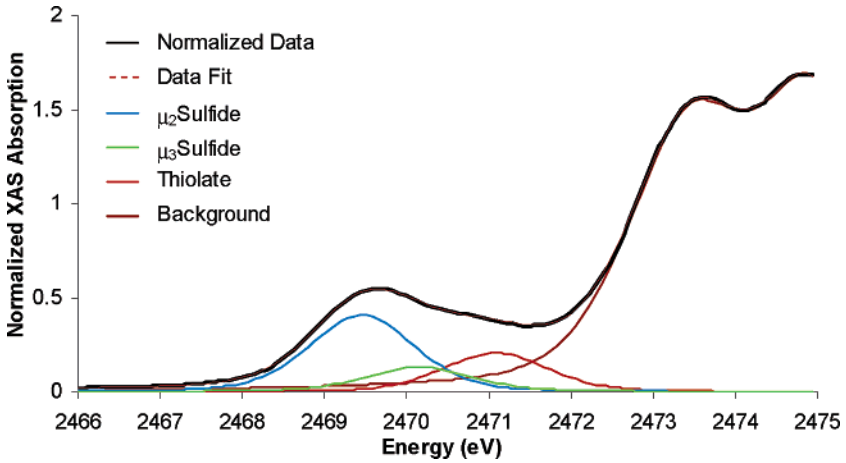

Figure 4. Components of $[Fe_3S_4]$ model complexes $[Fe_3S_4(LS_3)]^{3-}$. Normalized data (black solid line), fitted data (red dashed line), μ_2Sulfide (blue solid line), μ_3Sulfide (green solid line), thiolate (red solid line), and background (bold red solid line).

Table 1. Pre-edge Energies and Metal−Ligand Bond Covalencies of $[Fe^{3+}{}_2S_2Cl_4]^{2-}$, $[Fe^{2.5+}{}_4S_4Cl_4]^{2-}$, $[Fe^{3+}{}_2S_2(SPh)_4]^{2-}$, and $[Fe^{2.5+}{}_4S_4(SPh)_4]^{2-a}$

	pre-edge energy (eV)	covalency per metal–ligand bond (%)
$[Fe^{3+}{}_2S_2Cl_4]^{2-}$	2469.5	68
$[Fe^{2.5+}{}_4S_4Cl_4]^{2-}$	2470.1	39
$[Fe^{3+}{}_2S_2(SPh)_4]^{2-}$	2470.7	36
$[Fe^{2.5+}{}_4S_4(SPh)_4]^{2-}$	2470.8	36

[a] Determined from the minima of the second derivative of the normalized S K-edge XAS of these complexes.

→ Fe 3d transitions due to its presence in the $[Fe_3Se_4(LS_3)]^{3-}$ complex. The μ_2- and $\mu_3S_{sulfide}$ components contribute to the broad lower energy region in the asymmetric second derivative from 2468 to 2470 eV (Figure 2, dotted orange).

To resolve the contributions for the $\mu_2S_{sulfide}$ and $\mu_3S_{sulfide}$ to the pre-edge the following procedure was applied. The pre-edge feature of the complex $[Fe_4S_4Cl_4]^{2-}$ having all $\mu_3S_{sulfide}$ atoms ligated to $Fe^{2.5+}$ is at 2470.1 eV (Figure 3 dotted black), while the pre-edge feature of the complex $[Fe_2S_2Cl_4]^{2-}$ having all $\mu_2S_{sulfide}$ ligated to Fe^{3+} is at 2469.5 eV (Figure 3, black line).[21,25] The observed shift in the pre-edge energy position (0.6 eV) has contributions from the difference in 1s orbital energy of $\mu_2S_{sulfide}$ in $[Fe_2S_2Cl_4]^{2-}$ relative to that of $\mu_3S_{sulfide}$ in $[Fe_4S_4Cl_4]^{2-}$ and from the energy difference between the Fe^{3+} and $Fe^{2.5+}$ d-manifolds of these two complexes. An estimate of this d-manifold energy difference can be obtained from the pre-edge energy difference of $[Fe^{3+}{}_2Se_2(SPh_4)]^{2-}$ and $[Fe^{2.5+}{}_4Se_4(SPh_4)]^{2-}$ (Figure 3).[25,21] The metal−ligand bond covalencies (36%, Table 1) are the same in these complexes indicating similar charge transfer to the metal and thus equivalent 1s orbital energies of the $S_{thiolate}$. The observed pre-edge shift, 0.1 eV lower in $[Fe^{3+}{}_2Se_2(SPh_4)]^{2-}$ relative to $[Fe^{2.5+}{}_4Se_4(SPh_4)]^{2-}$, then provides an estimate of the orbital energy difference between Fe^{3+} and $Fe^{2.5+}$ (Fe^{3+} being lower) in these complexes, which reflects a combination of contributions from differences in ligand field and Z^{eff} on the metal.[37] Hence the $\mu_2S_{sulfide}$ 1s orbital energy in $[Fe_2S_2Cl_4]^{2-}$ is estimated to be about 0.5 eV higher than the $\mu_3S_{sulfide}$ 1s orbital energy of $[Fe_4S_4Cl_4]^{2-}$. The 1s orbital energy of the $\mu_3S_{sulfide}$ in the $[Fe_3S_4(LS_3)]^{3-}$ complex will be further lowered relative to the $[Fe_4S_4Cl_4]^{2-}$ complex as the $\mu_3S_{sulfide}$ will donate more charge to the Fe^{3+} present in $[Fe_3S_4(LS_3)]^{3-}$. Similarly, the 1s orbital energy of the $\mu_2S_{sulfide}$ will be higher in $[Fe_3S_4(LS_3)]^{3-}$ than in $[Fe_2S_2Cl_4]^{2-}$, as it will donate less charge to the $Fe^{2.5+}$ present in $[Fe_3S_4(LS_3)]^{3-}$. Thus the pre-edge contribution of $\mu_3S_{sulfide}$ should be at least ~0.5 eV higher in energy than that of the $\mu_2S_{sulfide}$ in $[Fe_3S_4(LS_3)]^{3-}$, as the transitions from both types of sulfides are to the same metal d-manifold.

The experimental spectrum was fit to obtain the pre-edge intensities of the $\mu_2S_{sulfide}$, $\mu_3S_{sulfide}$, and $S_{thiolate}$ components (Figure 4). The integrated intensities of the fit (Table 2) give the covalencies of each type of Fe−S bond involved (total % hole covalencies divided by number of ligand−metal bonds). The average Fe-$\mu_2$sulfide, $\mu_3$sulfide, and $S_{thiolate}$ bond covalencies are 56%, 39%, and 36%, respectively. For $[Fe_3Se_4(LS_3)]^{2-}$ the average Fe−$S_{thiolate}$ bond covalency is 27%. The decrease in thiolate covalency in the Se model complex indicates that the sulfide is a poorer donor to Fe than selenide resulting in higher charge transfer from $S_{thiolate}$ in $[Fe_3S_4(LS_3)]^{3-}$. This is also reflected in the pre-edge energy position of the $S_{thiolate}$ contribution in $[Fe_3S_4(LS_3)]^{3-}$ which is 0.1 eV higher than that for

Table 2. Experimental Metal−Ligand Bond Covalencies of $[Fe_3S_4]$ Model Complex and proteins

	$\mu_2S_{sulfide}$		$\mu_3S_{sulfide}$		$S_{thiolate}$	
	% covalency[a]	energy position	% covalency[a]	energy position	% covalency[a]	energy position
Model Complex						
$[Fe_3S_4(LS)_3]^{3-}$ $[Fe_3S_4]^0$	56 ± 1	2469.4	39 ± 1	2470.2	36 ± 1	2471.0
$[Fe_3Se_4(LS)_3]^{3-}$ $[Fe_3Se_4]^0$					29 ± 1	2470.9
Ferredoxin II from *D. gigas* (5 H-Bond to μ-2 Sulfides, 3H-bond to $S_{thiolate}$)						
$[Fe_3S_4(S\text{-}Cys)]^{3-}$ $[Fe_3S_4]^0$	25 ± 2	2469.7	28 ± 3	2470.2	24 ± 1	2470.9
$[Fe_3S_4(S\text{-}Cys)]^{3-}$ $[Fe_3S_4]^+$	38 ± 2	2469.4	38 ± 2	2470.0	38 ± 1	2470.6

[a] Total hole covalency per metal ligand bond.

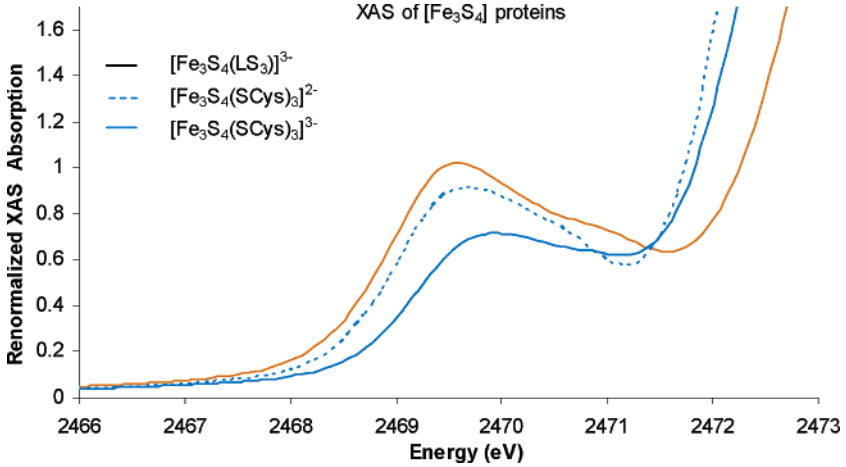

Figure 5. Renormalized S K-edge XAS of model complex $[Fe_3S_4(LS_3)]^{3-}$ (orange solid line) and oxidized (blue solid line) and reduced (blue dashed line) ferredoxin II from *D. gigas*.

$[Fe_3Se_4(LS_3)]^{3-}$. It should be noted that although the contributions from the different sulfur 1s donors could be resolved, the relative pre-edge contribution Fe^{3+} and contributions for the transitions to the two $Fe^{2.5+}$ could not. Thus the bond covalencies reported above are their average. DFT calculation on the cluster will be used to distribute the $Fe^{2.5+}$ and Fe^{3+} bonding contributions (vide infra).

B. S K-Edge of Protein Active Sites. The S K-edge spectra of the protein ferredoxin II from *D. gigas* in the resting $[Fe_3S_4]^0$ form (same redox state as the model) and the oxidized $[Fe_3S_4]^+$ form are given in Figure 5. The resting protein spectrum (solid blue in Figure 5) shows a broad pre-edge feature similar to that of the model (solid orange in Figure 5) but with less intensity. The fit to the experimental reduced protein spectrum (Figure 6b) allows the intensity decrease to be distributed over the $\mu_2S_{sulfide}$, $\mu_3S_{sulfide}$ and $S_{thiolate}$ components. The bond covalencies (Table 2) decrease from 55%, 32% and 36% in the model to 25%, 28% and 24% for the Fe-$\mu_2S_{sulfide}$, Fe-$\mu_3S_{sulfide}$, and Fe−$S_{thiolate}$ bonds, respectively, in the protein active site in the same oxidation state. Note that the decrease is largest for the $\mu_2S_{sulfide}$ and least for the $\mu_3S_{sulfide}$. These results will be discussed in the context of protein effects on bonding.

The S K-edge spectrum of the oxidized protein site shows an increase in pre-edge intensity relative to that of the reduced state (dashed vs bold blue, respectively, in Figure 5). Since oxidation involves creation of a hole, the pre-edge intensity is expected to increase. Based on the covalencies of the $[Fe_3S_4]^0$ state (25%, 28%, and 24% for Fe-$\mu_2S_{sulfide}$, Fe-$\mu_3S_{sulfide}$, and Fe−$S_{thiolate}$, respectively), the increase from 14 to 15 holes on oxidation should increase the covalencies to 27%, 30%, and 24%, respectively. However, the results of the fit (Table 2) show that the individual bond covalencies in the oxidized state increase by more than this factor (38%, 38%, and 38% for Fe-$\mu_2S_{sulfide}$, Fe-$\mu_3S_{sulfide}$, and Fe−$S_{thiolate}$, respectively). Also DFT calculations (vide infra) on the resting $[Fe_3S_4]^0$ form show that the redox active molecular orbital (RAMO) has no $\mu_3S_{sulfide}$ component (vide infra), while the experimental results show that the covalencies of all three components ($\mu_2S_{sulfide}$, $\mu_3S_{sulfide}$, and $S_{thiolate}$) increase on oxidation. These deviations from the ground state predictions may indicate that electronic relaxation is involved in the redox process in this cluster and this is evaluated below using DFT calculations.[26]

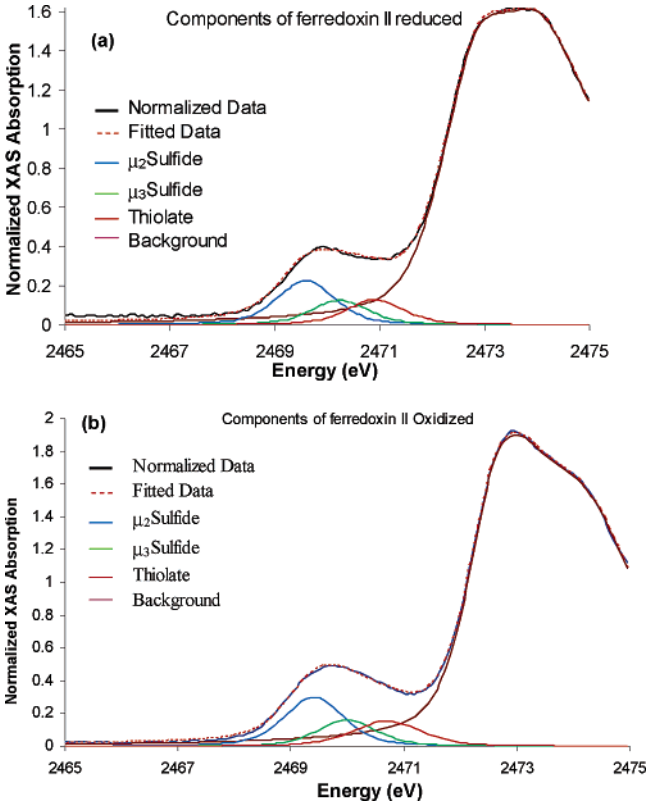

Figure 6. Components of $[Fe_3S_4]$ protein ferredoxin II oxidized (a) and reduced (b). Normalized data (black solid line), fitted data (red dashed line), μ_2Sulfide (blue solid line), μ_3Sulfide (green solid line), thiolate (red solid line), and background (bold red solid line).

Analysis

A. DFT Optimized Geometric and Electronic Structure. Geometry-optimized DFT calculations were performed on the truncated structure $[Fe_3S_4(SMe)_3]^{3-}$ to correlate to the S K-edge data on the model complex. The optimized structure exhibits overall reasonable agreement with the reported crystal structure of the $[Fe_3S_4LS_3]^{3-}$ model complex (Figure 7).[27] The optimized structure shows a small expansion of the core, as reflected by slightly longer (0.03 Å) Fe−Fe and Fe−S_s distances. There is also an increase of about 0.05−0.08 Å in the Fe−$S_{thiolate}$ distances in the optimized structure as compared to the crystal structure. This has contributions from the GGA functional used

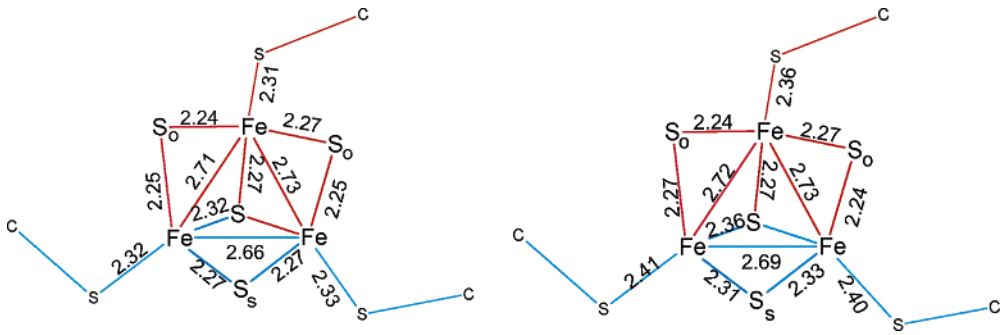

Figure 7. Crystal structure (a) and geometry optimized structure (b) of $[Fe_3S_4]^0$ cluster. S_s is the bridging sulfide in the $[Fe_2S_2]^+$ subsite, while S_o is the sulfide bridging the $Fe^{2.5+}$'s to the Fe^{3+}.

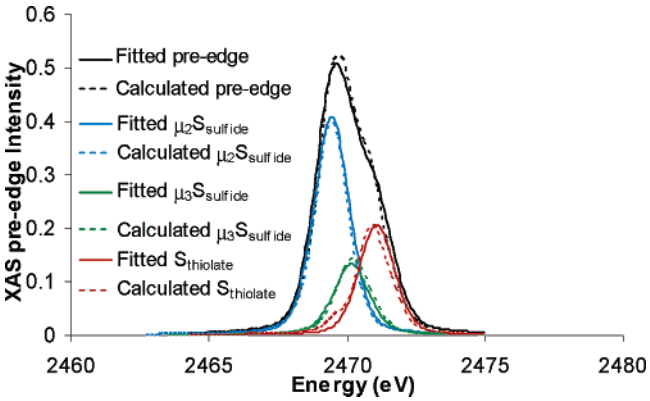

Figure 8. DFT calculated density of states (DOS) (in dotted lines) compared to experimentally observed DOS (in solid lines) for $\mu_2S_{sulfide}$ (blue), $\mu_3S_{sulfide}$ (green), and $S_{thiolate}$ (red). The relative energy positions of calculated DOS are determined from the relative experimental pre-edge positions of the components, and their calculated covalencies are rescaled by the factors they are off from in experiment (Table 4).

(the calculated bond lengths in $Fe(SR)_4^{-/2-}$ are 0.05−0.07 Å longer than those in reported crystal structures using the same level of theory) and constraints imposed by the bulky tris-arylthiolate ligand.[38]

The calculated bond covalencies (total hole covalency of a donor ligand divided by number of Fe-donor ligand bonds) for $\mu_2S_{sulfide}$, $\mu_3S_{sulfide}$, and $S_{thiolate}$ are 35%, 24%, and 20%, respectively, which are a factor of 1.5 to 1.8 less than their experimentally observed total hole covalencies of 53%, 39%, and 36%, respectively (Table 2), for the model complex. A similar underestimation of covalency by using a pure density functional has also been found in DFT calculations of Fe_4S_4 clusters.[26] In terms of per hole per ligand covalency, this difference corresponds to a 2% decrease in the calculations.

Though the calculated covalency is less than the experimentally determined covalency, the density of states (DOS) estimated from the DFT calculation on the optimized structure agrees well with the experimental pre-edge features (Figure 8). This indicates that the DFT calculations, although quantitatively underestimating the bonding in this cluster, give a reasonable description of the relative contributions of the different types of sulfur to the electronic structure description in the $[Fe_3S_4(LS_3)]^{3-}$ cluster.

A schematic energy diagram of the cluster showing the energy levels involved in the redox process is given in Figure 9. The reduced ground state has 10 α electrons and 1 β electron in the delocalized $[Fe_2S_2]^+$ subsite (in red) and 5 β electrons localized on the high-spin Fe^{3+} center (in blue). For clarity only the contours of the orbitals 1β (the delocalized β Fe $d_{x^2-y^2}$ + Fe $d_{x^2-y^2}$ bonding orbital), 1α (α HOMO-1), 2α (HOMO), and 2β (LUMO) are shown. Note that the bonding and the antibonding orbitals on Fe^{3+} are energetically well separated from the HOMO and LUMO and hence are not considered in the following analysis. The HOMO-1 (1α), HOMO (2α), and the LUMO (2β) are antibonding orbitals centered on the delocalized $[Fe_2S_2]^+$ subsite of the cluster. The $\mu_2S_{sulfide}$, $\mu_3S_{sulfide}$, and $S_{thiolate}$ contributions are 38%, 15%, and 3% in the HOMO-1; 39%, 4%, and 15% in the HOMO; and 5%, 2%, and 0% in the LUMO, respectively (Figure 9). The short Fe−Fe distance in this cluster (2.69 Å), compared to the Fe−Fe distance in reduced $[Fe_2S_2]^+$ clusters (2.73 Å), has a significant effect on the MO description of the $[Fe_3S_4]^0$ cluster relative to the $[Fe_2S_2]^+$ cluster. The strong Fe−Fe interaction causes the β Fe $d_{x^2-y^2}$ + Fe $d_{x^2-y^2}$ bonding orbital (1β in Figure 9) to be stabilized and the β Fe $d_{x^2-y^2}$ − Fe $d_{x^2-y^2}$ antibonding orbital (2β LUMO in Figure 9) to be destabilized. This is the reason the HOMO is the 2α Fe $d_{x^2-y^2}$ − Fe $d_{x^2-y^2}$ antibonding orbital rather than the 1β Fe $d_{x^2-y^2}$ + Fe $d_{x^2-y^2}$ bonding orbital which is the HOMO in a delocalized Fe_2S_2 cluster (Figure 9).[16] Note that the HOMO which is the redox active molecular orbital (RAMO) (2α in Figure 9) does not have significant $\mu_3S_{sulfide}$ character. However the experimental results (Table 2) clearly show an increase in $\mu_3S_{sulfide}$ covalency upon oxidation. This implies that there is electronic relaxation which changes the wave function on oxidation.

B. Bonding in the $[Fe_3S_4]^0$ Cluster. The S K-edge results on the resting state model $[Fe_3S_4(LS_3)]^{3-}$ (Table 2) give the average (Fe^{3+}+2$Fe^{2.5+}$) $\mu_2S_{sulfide}$, $\mu_3S_{sulfide}$, and $S_{thiolate}$ covalencies as 56%, 39%, and 36%, respectively. Previous studies have determined the covalency of an $Fe^{2.5+}$−$\mu_2S_{sulfide}$ to be 61% (for $[Fe_2S_2]^+$), $Fe^{2.5+}$−$\mu_3S_{sulfide}$ to be about 39% (in $[Fe_4S_4Cl_4]^{2-}$), and both Fe^{3+}−$S_{thiolate}$ and $Fe^{2.5+}$−$S_{thiolate}$ to be 36% (in $[Fe_2Se_2(SPh)_4]^{2-}$ and $[Fe_4S_4(SPh)_4]^{2-}$, respectively). However the covalencies observed reflect an average of two $Fe^{2.5+}$ and one Fe^{3+}(a better charge acceptor than $Fe^{2.5+}$). DFT calculations were used to distribute the experimental total hole covalencies into Fe^{3+} and $Fe^{2.5+}$ components.

The calculated Fe^{3+} and $Fe^{2.5+}$ components of each individual type of donor ligand (Table 3) were scaled up by the ratio of total experimental to total calculated hole covalency. This gives experimental estimates of the Fe^{3+} covalencies as 64%, 53%, and 41% for $\mu_2S_{sulfide}$, $\mu_3S_{sulfide}$, and $S_{thiolate}$ bonds, respectively. The corresponding $Fe^{2.5+}$ covalencies are 46%, 31%, and 34%, respectively.[39] The $Fe^{2.5+}$-$\mu_3S_{sulfide}$ covalency in the $[Fe_3S_4]^0$ cluster has decreased significantly to 31% from 39% in the $[Fe_4S_4]^{2+}$ cluster[21] due to both the stronger charge donation by

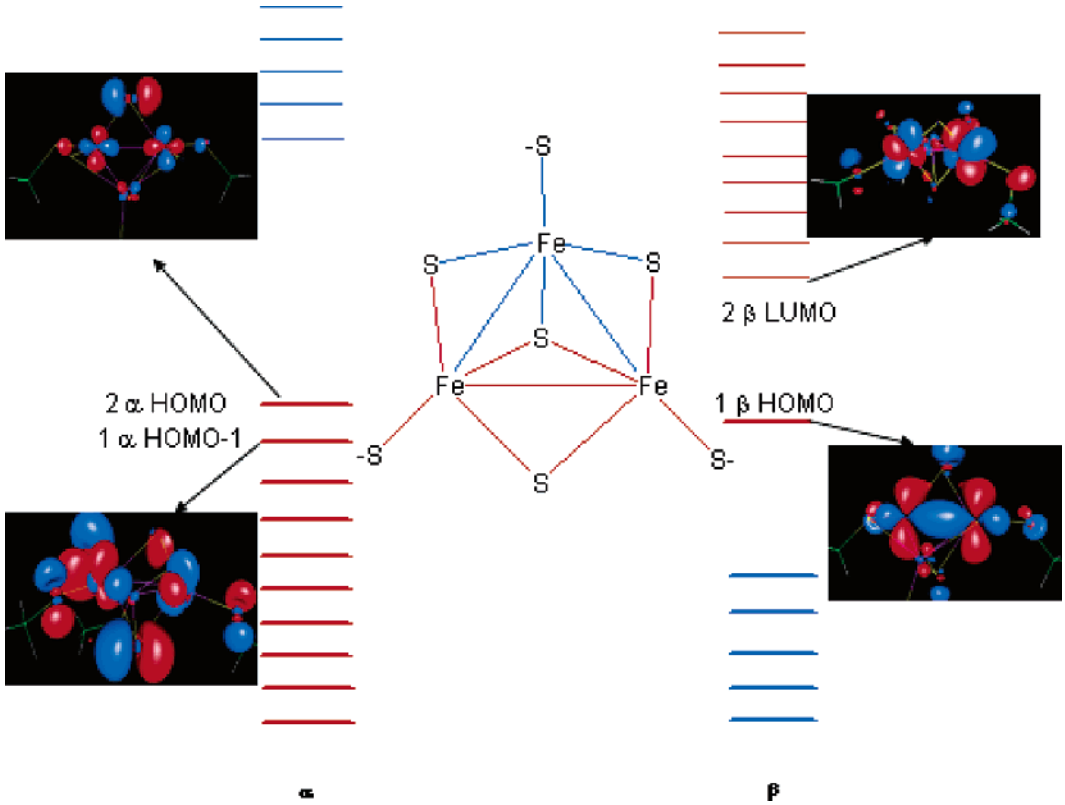

Figure 9. Schematic diagram of a reduced $[Fe_3S_4]$ cluster. The $[Fe_2S_2]$ subsite (in red) has 10 occupied α orbitals (bold red) with HOMO and the HOMO-1 marked as 2α and 1α, respectively. It has an occupied delocalized β orbital 1β (which is HOMO in bold red). The unoccupied β orbitals (in red) have 2β as the β LUMO. The Fe^{3+} center has 5 occupied β orbitals (in bold blue) and 5 unoccupied α orbitals (in blue). They are energetically separated from the Fe_2S_2 subsite orbitals. The numbers (in %) above and below the orbital picture indicate their μ_3S, μ_2S, and $S_{thiolate}$ coefficients in reduced ground state.

Table 3. Calculated Per Metal−Ligand Bond Covalencies and Experimental Covalencies Divided into Fe^{3+} and $Fe^{2.5+}$ Components (in Italics) Using the Calculated Results

	$\mu_2S_{sulfide}$			$\mu_3S_{sulfide}$			$S_{thiolate}$		
	Fe^{3+}	$Fe^{2.5+}$	total	Fe^{3+}	$Fe^{2.5+}$	total	Fe^{3+}	$Fe^{2.5+}$	total
$[Fe_3S_4]^0$ experimental, extrapolated	*64*	*46*	56	*53*	*31*	39	*36*	*36*	36
$[Fe_3S_4]^0$ optimized, calculated	41	29	35	57	19	24	20	20	20

Table 4. Values of *J*, *B*, and $\lambda^2/2k$ Obtained from Experimental Covalencies, DFT, and Resonance Raman Studies, Respectively

	Fe–S covalency			estimate	estimate	estimate	
	μ_3, %	μ_2, %	avg, %	of *J*, cm^{-1}	of *B*, cm^{-1}	of $\lambda^2/2k$, cm^{-1}	*B*/2*J*
$[Fe_2S_2]^+$ localized		61	61	−360	875	3660	1.34
$[Fe_2S_2]^+$ $[Fe_3S_4]^0$	31	46	39	−147	1600	3660	5.16

the $\mu_3S_{sulfide}$ to the Fe^{3+} center and also the strong competitive charge donation by the $\mu_2S_{sulfide}$ decreasing its charge transfer to the $Fe^{2.5+}$centers. The strong $\mu_2S_{sulfide}$ charge donation also decreases the charge transfer from the other $\mu_2S_{sulfide}$, as the covalency of the $Fe^{2.5+}$−μ_2S bond (48%) and Fe^{3+}−μ_2S bond (64%) (Table 3) observed here are less than their values of 61%[21] for $Fe^{2.5+}$−μ_2S and 88%[25] for Fe^{3+}−μ_2S, respectively.

It is important to emphasize that the covalency of the bridging sulfide ligands of the redox active $[Fe_2S_2]^{1+}$ subsite of $[Fe_3S_4]^0$ has decreased to 39% (average of $\mu_2S_{sulfide}$ (48%)+ $\mu_3S_{sulfide}$ (31%)) from 61% in the reduced Fe_2S_2 cluster.[21] This will have a significant effect on the delocalization within the $[Fe_2S_2]^{1+}$ subsite as evaluated below.

C. Delocalization in the $[Fe_2S_2]^+$ Subsite of the $[Fe_3S_4]^0$ Cluster. In this section *J*, *B*, and $\lambda^2/2k$ in eq 1 will be estimated from experimental results and DFT calculations to evaluate their contributions to the delocalization of the $[Fe_2S_2]^+$ subsite of $[Fe_3S_4]^0$.

Superexchange Coupling Constant, *J*: The effect of the decrease in the covalency of the bridging ligand of the $[Fe_2S_2]^+$ subsite of the $[Fe_3S_4]^0$ cluster on the energies of the different spin states can be estimated by using an approximate relationship between the phenomenological superexchange coupling constant, *J*, and the covalency of the metal ions with the bridging ligands (eq 2).[21]

The exchange coupling in reduced $[Fe_2S_2]^+$ was determined to be $J = -360$ cm^{-1} (this is the pure superexchange contribution, corrected for double exchange and vibronic coupling),[20] and its bridging ligand covalency was estimated in ref 15 to be 61%. The bridging sulfide covalency in the $[Fe_2S_2]^+$ subsite of the $[Fe_3S_4]^0$ cluster is determined here to be 39% (Table 4, using the average of μ_2 and μ_3 bridges). The *J* for the $[Fe_2S_2]^+$ subsite of the $[Fe_3S_4]^0$ cluster is thus estimated to be -146 cm^{-1}.

Double Exchange Parameter, *B*: The double exchange parameter *B* is calculated, using DFT, from the ground-state energy difference of the bonding and antibonding combinations of the Fe 3d orbitals on the two metal centers representing the direct σ delocalization pathway (this is obtained from the energy

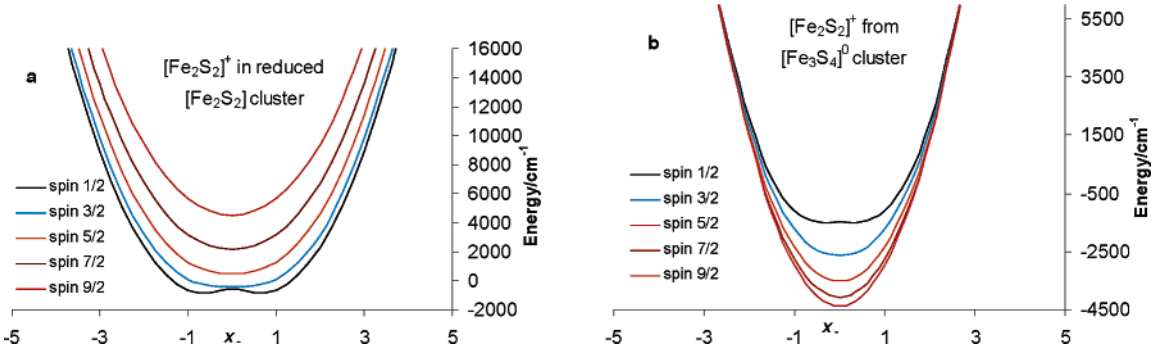

Figure 10. Potential energy surface of different spin states in the (a) reduced Fe_2S_2 and (b) reduced $[Fe_3S_4]^0$ cluster using eq 1.

Scheme 1. Flowchart Showing the Changes in Calculated Total Hole Covalencies (Expressed As Ratios to the Reduced Hole Covalency) of Individual Components along the Redox Pathway in a $[Fe_3S_4]$ Cluster (the Protein Ratio Is the Experimentally Observed Value)

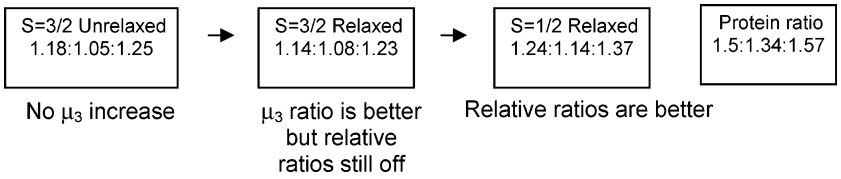

splitting of the 1β and 2β orbitals in Figure 9). The calculated values of B are 1550 and 850 cm^{-1} [40] for an $[Fe_2S_2]^+$ subsite of $[Fe_3S_4]^0$ and the $[Fe_2S_2]^+$ cluster, respectively. The higher B in the $[Fe_2S_2]^+$ subsite of the $[Fe_3S_4]^0$ cluster is due to shortening of its Fe−Fe distance from 2.73 Å in the Fe_2S_2 cluster to 2.66 Å in the subsite, which allows for a stronger Fe−Fe interaction and thus a higher B. The value of B for the Class III valence delocalized complex $[Fe_2(OH)_3(tmtacn)_2]^{2+}$ has been experimentally determined to be 1350 cm^{-1}.[20] The DFT calculated value for the same complex is 1300 cm^{-1}. This experiment-to-calculated ratio is then used to scale the calculated values of the $[Fe_2S_2]^+$ sites to obtain calibrated estimates of the B values (Table 4).

Vibronic Coupling Parameter, $\lambda^2/2k$: The value of the vibronic coupling parameter $\lambda^2/2k$ has been experimentally determined from resonance Raman spectra for $[Fe_2S_2]^+$ [41] and $[Fe_4S_4]^{2+}$ [4] clusters which were used to estimate the effective frequency of the x_- mode representing the antisymmetric combinations of local breathing modes of the $[Fe_2S_2]^+$ subsite of the cluster.[21] While the appropriate resonance Raman data for the $[Fe_3S_4]^0$ cluster does not exist, the vibronic coupling is likely to be similar to that of the $[Fe_2S_2]^+$ subsite of the $[Fe_4S_4]^{2+}$ cluster (3190 cm^{-1}) as the geometric structures of these $[Fe_2S_2]^+$ subsites are quite similar. Here we use the vibronic coupling value for the reduced $[Fe_2S_2]^+$ cluster (3660 cm^{-1}) as it provides an upper limit for this analysis, making the system harder to delocalize.[42]

Potential Energy Surfaces (PES) of the Different Spin States: With estimates of the superexchange parameter (J), double exchange parameter (B), and the vibronic coupling constant ($\lambda^2/2k$), the potential energy surfaces of the different spin states of the reduced $[Fe_2S_2]^+$ cluster (Figure 10 A) and of the $[Fe_2S_2]^+$ subsite of the $[Fe_3S_4]^0$ cluster (Figure 10 B) were obtained using eq 1. The analysis shows that the ground state of the $[Fe_2S_2]^+$ unit of $[Fe_3S_4]^0$ cluster is a delocalized $S = {}^9/_2$ state. This delocalization as observed experimentally[9] results from a simultaneous decrease in J and increase in B relative to their values in the reduced Fe_2S_2 cluster in which the larger J and smaller B stabilize the localized $S = {}^1/_2$ ground state.

D. Change in Electronic Structure on Oxidation (Electronic Relaxation). From Table 2 the $\mu_2S_{sulfide}$, $\mu_3S_{sulfide}$, and the $S_{thiolate}$ contributions to the total hole covalencies increased by the ratios 1.5, 1.34, and 1.57, respectively, upon oxidation of the $[Fe_3S_4]^0$ cluster to the spin frustrated $[Fe_3S_4]^+$ $S = {}^1/_2$ final state.[8] However DFT results on the $[Fe_3S_4]^0$ ground state indicate that the RAMO (2α in Figure 9) does not contain significant $\mu_3S_{sulfide}$ character. Hence, on oxidation, the hole created cannot significantly increase the $\mu_3S_{sulfide}$ pre-edge intensity in contrast to the experimental results (calculated ratios 1.18, 1.05, and 1.25, Scheme 1). Also, on oxidation of the RAMO, an $S = {}^3/_2$ state (Scheme 1) is obtained (i.e., there are 9 α and 6 β electrons, Figure 9) which is not the final spin state of the oxidized form ($S = {}^1/_2$). On letting the system electronically relax (i.e., the electronic structure is allowed to change to charge compensate the hole produced on oxidizing the RAMO), the $\mu_3S_{sulfide}$ contribution increases and the relative intensity ratios (Scheme 1) now become 1.14, 1.08, and 1.23 for $\mu_2S_{sulfide}$, $\mu_3S_{sulfide}$, and $S_{thiolate}$, respectively. However the relative increase of the $\mu_3S_{sulfide}$ is still small relative to experiment, and the spin state is still $S = {}^3/_2$. To obtain an $S = {}^1/_2$ ground state, an additional spin forbidden transition from the now α HOMO (1α in Figure 9) of the $S = {}^3/_2$ oxidized state to the β LUMO (2β in Figure 9) also occurs. This creates a hole (1α in Figure 9) with 15% $\mu_3S_{sulfide}$ character and depletes a hole (2β in Figure 9) with 2% $\mu_3S_{sulfide}$ character leading to an overall increase in the $\mu_3S_{sulfide}$ character in the total hole covalency. This calculation corresponds to the oxidized site in the $S = {}^1/_2$ spin state as observed experimentally. Now the calculated ratios of increase in hole covalency are (Scheme 1) 1.24, 1.14, and 1.37 for $\mu_2S_{sulfide}$, $\mu_3S_{sulfide}$, and $S_{thiolate}$, respectively, for this $S = {}^1/_2$ oxidized cluster. Though these ratios are still low relative to experiment, their relative magnitudes parallel the experimental results. One contribution to this difference between the calculated and observed change is the differential effect of the protein environment (see below) on the covalencies of the oxidized and reduced clusters.[43] H-bonding, in the protein will more significantly affect the reduced cluster as it has increased charge density. This will increase

the ratio of the total hole covalencies of oxidized to reduced relative to the values calculated for an isolated cluster.

Discussion

A. Effect of Protein Environment. The experimentally observed total $\mu_2S_{sulfide}$, $\mu_3S_{sulfide}$ and $S_{thiolate}$ hole covalencies in the $[Fe_3S_4(LS_3)]^{3-}$ model complex are 56%, 39% and 36%, respectively (Table 2). However, the experimentally observed total hole covalencies of the corresponding protein active site in the same redox state $[Fe_3S_4(S-Cys)_3]^{3-}$ are 25%, 28% and 24%, respectively (Table 2). This decrease in the observed total hole covalency in the protein active site compared to the model complex (Figure 5) can have contributions from incomplete loading of the active site[44] and differences in structure imposed by the tri-arylthiolate ligand relative to the protein. However, it is important to note that the decrease of pre-edge intensity of the $\mu_2S_{sulfide}$ of the protein active site relative to model is much larger than that of the $\mu_3S_{sulfide}$ and $S_{thiolate}$ (a factor of 0.44 vs., 0.77 vs 0.67, respectively).[45] Similar decreases in metal ligand bond covalencies in the Fe−S active sites of 1Fe rubredoxins, and 2Fe and 4Fe ferredoxins have been previously reported.[25,26] H-bonding in the protein will decrease the ligand−metal bond covalency by stabilizing the charge density on the ligand. The mononuclear rubredoxin site had 4−6 H-bonds which reduced the Fe−S bond covalency from 37% in the model to 31% in the protein active site. The decrease was even large for the $\mu_2S_{sulfide}$−Fe bond (88% to 77% with 2−4 H-bonds) probably due to increased charge density on the sulfide. The Fe_3S_4 active site of ferredoxin II from *D. gigas* has 5 backbone NH$\cdots$ $\mu_2S_{sulfide}$, 3 backbone NH$\cdots S_{thiolate}$ H-bonds, and no H-bonds to the $\mu_3S_{sulfide}$.[28] Hence, the expected relative decrease of covalency is $\mu_2S_{sulfide} > S_{thiolate} > \mu_3S_{sulfide}$.[46,47] Experimentally, the observed decrease reflects this order suggesting that H-bonding makes a major contribution to the reduction of $\mu_2S_{sulfide}$−Fe bond covalency in the protein active site. This decrease in ligand−metal bond covalency in the protein relative to the model complex in the same oxidation state will stabilize the reduced $[Fe_3S_4]^0$ state of the cluster more than its one-electron oxidized form and will significantly contribute to the observed shift of the reduction potential of the $[Fe_3S_4]^{0/+}$ couple from −790 mV in the model to −130 mV in the protein.[27,48,49]

B. Bonding and Delocalization in the Fe_3S_4 Cluster. The general bonding within an $[Fe_3S_4]^0$ cluster (Figure 9) is described as an Fe^{3+} center antiferromagnetically coupled to the $Fe^{2.5+}$−$Fe^{2.5+}$ delocalized subsite. The bonding description obtained for the Fe^{3+} site (vide supra) shows that the $Fe^{3+}-S_{thiolate}$ covalency (36%) is similar to that obtained for Fe^{3+} tetrathiolates (42%); however the $Fe^{3+}-\mu_2S_{sulfide}$ bond covalency (56%) is much lower than that observed for oxidized $[Fe_2S_2]^{2+}$ clusters (88%) due to its ligation to three competing sulfides compared to two in $[Fe_2S_2]^{2+}$. With respect to the $[Fe^{2.5+}{}_2S_2]^+$ unit of the $[Fe_3S_4]^0$ cluster, the bonding is quite different from that of the reduced $[Fe_2S_2]^+$ site and the $[Fe_2S_2]^+$ subsite of the $[Fe_4S_4]^{2+}$ cluster with respect to $\mu_2S_{sulfide}$ and $\mu_3S_{sulfide}$ covalencies, respectively. The Fe−$\mu_2S_{sulfide}$ bond covalency was estimated to be 61% in a reduced $[Fe_2S_2]^+$ cluster, while for the $[Fe_2S_2]^+$ subsite of $[Fe_3S_4]^0$ this is greatly reduced to 46%. This results from the strong charge donation by the other ligated $\mu_2S_{sulfide}$ (Figure 1). The Fe−$\mu_3S_{sulfide}$ bond covalency in the $[Fe_2S_2]^+$ subsite of $[Fe_3S_4]^0$ (31%) is also less than that of the Fe−$\mu_3S_{sulfide}$ bond covalency in the $[Fe_2S_2]^+$ subsite of $[Fe_4S_4]^{2+}$ (39%). This also reflects the stronger charge donation by the $\mu_2S_{sulfides}$ and the preferential charge donation of the $\mu_3S_{sulfide}$ to the Fe^{3+} center (Figure 1).

These effects reduce the bridging covalency and thus decrease the superexchange, J, between these two $Fe^{2.5+}$ centers. This decrease in J, coupled to the increase in B, due to the decreased $Fe^{2.5+}-Fe^{2.5+}$ bond length in the $[Fe_3S_4]^0$ cluster (similar to that of the $[Fe_4S_4]^{2+}$ cluster), changes the potential energy surface (PES) of the different spin states (Figure 10, according eq 1).

It shows that the ground state of the reduced $[Fe_2S_2]^+$ cluster is predicted to be $S = {}^1/_2$, while that for the $[Fe_2S_2]^+$ subsite of the $[Fe_3S_4]^0$ cluster should be $S = {}^9/_2$. Though spin frustration can make a significant contribution to the energies of different spin states of these clusters,[50] these results indicate that the unique bonding features of the $[Fe_2S_2]^+$ subsite of the $[Fe_3S_4]^0$ cluster (i.e., replacing the thiolates of $[Fe_2S_2(SR)_4]^{2-}$ by $\mu_2S_{sulfide}$ in $[Fe_3S_4]^0$) can alone stabilize a valence delocalized $S = {}^9/_2$ ground state in the $[Fe_2S_2]^+$ subsite.

C. Two Step Oxidation Process in Fe_3S_4: Ionization and Spin Flip. The S K-edge XAS data on the oxidized protein clearly indicate an increase in $\mu_3S_{sulfide}$ contribution upon oxidation (Figure 5). Such an increase is **not** predicted by DFT calculations on the resting ground state, as these show no significant μ_3S_{sufide} character in the RAMO (2α HOMO in Figure 9). This increase in $\mu_3S_{sulfide}$ character in the resting oxidized state reflects the fact that the redox process in a $[Fe_3S_4]^0$ cluster involves two steps. The first involves removal of an electron from the HOMO of the cluster (2α localized on the Fe_2S_2 subsite Figure 9) giving first an $S = {}^3/_2$ excited state. This process increases the hole covalencies of $\mu_2S_{sulfide}$ and $S_{thiolate}$ (as seen in the pre-edge intensity increase in Figure 5); however, as the $\mu_3S_{sulfide}$ character in the HOMO is insignificant, the $\mu_3S_{sulfide}$ hole covalency cannot increase in this step even after electronic relaxation. The second step involves the transition of an electron from the α HOMO of the $S = {}^3/_2$ oxidized state (1α in Figure 9), which has significant $\mu_3S_{sulfide}$ character, into the 2β LUMO, which has negligible $\mu_3S_{sulfide}$ character, and requires spin−orbit coupling. This gives the experimentally observed $S = {}^1/_2$ final state and also provides an explanation of the increase in the $\mu_3S_{sulfide}$ covalency upon oxidation in Figure 5 and Table 2.

D. Possible Functional Relevance of the Redox Silent Fe^{3+} Site. As discussed above, the redox process of an $[Fe_3S_4]^0$ cluster is localized on the $[Fe_2S_2]^+$ unit. However the third Fe^{3+} center can facilitate this process on the $[Fe_2S_2]^+$ subsite through exchange coupling. Oxidation of an isolated Class III valence delocalized $[Fe_2S_2]^+$ unit should, upon removal of the single delocalized electron, produce an $S = 5$ state. However the very covalent bridging sulfides stabilize the antiferromagnetically coupled $S = 0$ ground state.[10] So the $S = 5$ excited state of the oxidized cluster must relax to an $S = 0$ state. This requires five spin flips each made possible by spin−orbit coupling. In an $[Fe_2S_2]^{2+}$ cluster the intermediate $S = 5$ and final $S = 0$ oxidized states have an energy gap (ΔE) of approximately 0.9 eV (Figure 11a). Hence this process will introduce an additional $\Delta G^{\ddagger}$ of this magnitude in an ET process involving these reduced ($S = {}^9/_2$) and oxidized ($S = 0$) states. This should be the case in a delocalized dimer. However, the presence of the third Fe^{3+} center in Fe_3S_4 changes the spin topology of the cluster. The highest spin state is all high spin, $S = {}^{15}/_2$, and the lowest spin

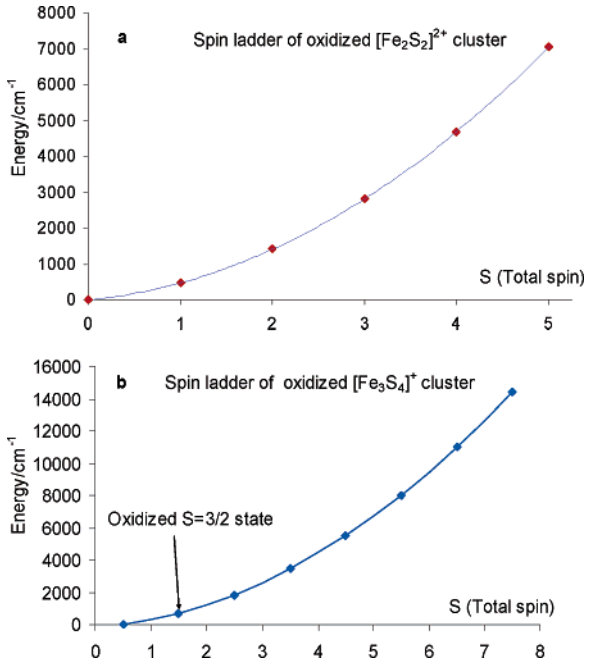

Figure 11. Calculated spin ladder for (a) $[Fe_2S_2]^{2+}$ (high spin $S = 5$ to low spin $S = 0$) and (b) $[Fe_3S_4]^{1+}$ (high spin $S = {}^{15}/_2$ to low spin $S = {}^1/_2$). Oxidation of reduced $[Fe_3S_4]^0$ cluster gives $S = {}^3/_2$ state.

state is $S = {}^1/_2$, the final oxidized state (Figure 11b). One-electron oxidation of the reduced $S = 2$ stateproduces an $S = {}^3/_2$ state in the trimer (oxidation of 2α in Figure 9).[51] The calculated spin ladder for an $[Fe_3S_4]^+$ cluster (Figure 11b) shows that relaxation to the final $S = {}^1/_2$ state from this intermediate $S = {}^3/_2$ state involves only one spin flip and has a ΔE of only 0.1 eV.[52] This greatly reduces the $\Delta G^{\ddagger}$ of this ET process. Thus the presence of the additional antiferromagnetic coupling to the Fe^{3+} center can contribute to the ET process of the $[Fe_2S_2]^+$ subsite in the Fe_3S_4 suggesting a possible functional role of the redox inactive Fe^{3+} center in the $[Fe_3S_4]$ cluster.

Acknowledgment. This research was supported by NSF CHE-9980549 (E.I.S.), NIH RR-01209 (K.O.H.), and by NIH GM 28856 (R.H.H.). Stanford Synchrotron Radiation Laboratory operations are funded by the U.S. Department of Energy, Office of Basic Energy Sciences. The SSRL Structural Molecular Biology Program is supported by the National Institutes of Health, National Center for Research Resources, Biomedical Technology Program, and by the U.S. Department of Energy, Office of Biological and Environmental Research.

Supporting Information Available: The expanded energy region plots of the data, the optimized *xyz* coordinates of the $[Fe_3S_4(SMe)_3]^{3-}$ complex, a sample input file used for ADF calculation and the rescaled protein vs model plot. This material is available free of charge via the Internet at http://pubs.acs.org.

JA0466208

(51) Due to the presence of antiferromagnetic coupling of the $S = {}^9/_2$ $[Fe_2S_2]^+$ with the Fe^{3+} ($S = {}^5/_2$) in the $[Fe_3S_4]^0$ cluster, the ground state of the reduced cluster is $S = 2$.

(52) Note that if the minority spin β electron from 1β (Figure 9) is oxidized which will be the case of a reduced delocalized $[Fe_2S_2]^+$ cluster, the intermediate oxidized state is an $S = {}^5/_2$ state which is separated from the final $S = {}^1/_2$ state by 0.25 eV. This barrier is still much less than the 0.9 eV separation for the reduced delocalized $[Fe_2S_2]^+$ cluster.